Membrane curvature regulates ligand-specific membrane sorting of GPCRs in living cells

Kadla R Rosholm[1,2,6], Natascha Leijnse[2,3], Anna Mantsiou[1,2], Vadym Tkach[1,2], Søren L Pedersen[2,4,6], Volker F Wirth[1,2], Lene B Oddershede[2,3], Knud J Jensen[2,4], Karen L Martinez[1,2], Nikos S Hatzakis[1,2,6], Poul Martin Bendix[3], Andrew Callan-Jones[5] & Dimitrios Stamou[1,2]*

The targeted spatial organization (sorting) of Gprotein-coupled receptors (GPCRs) is essential for their biological function and often takes place in highly curved membrane compartments such as filopodia, endocytic pits, trafficking vesicles or endosome tubules. However, the influence of geometrical membrane curvature on GPCR sorting remains unknown. Here we used fluorescence imaging to establish a quantitative correlation between membrane curvature and sorting of three prototypic class A GPCRs (the neuropeptide Y receptor Y2, the β_1 adrenergic receptor and the β_2 adrenergic receptor) in living cells. Fitting of a thermodynamic model to the data enabled us to quantify how sorting is mediated by an energetic drive to match receptor shape and membrane curvature. Curvature-dependent sorting was regulated by ligands in a specific manner. We anticipate that this curvature-dependent biomechanical coupling mechanism contributes to the sorting, trafficking and function of transmembrane proteins in general.

The targeted sorting of GPCRs into specialized membrane compartments is essential for their biological function[1,2]. Traditionally, the sorting of GPCRs has been attributed primarily to protein-mediated interactions[3]. However, recent findings have demonstrated that membrane physical properties have the capacity to regulate both GPCR activity[4,5] and localization[6,7]. High membrane curvature is a recurrent phenotype in specialized regions of the plasma membrane, such as filopodia in dendrites and microvilli in apical membranes[8], and in intracellular sorting compartments such as the endoplasmic reticulum, trafficking vesicles and endosome tubules[8–10]. However, the influence of geometrical membrane curvature[11] on GPCR sorting remains unknown. In this study we hypothesized that geometrical curvature is not a passive feature of cellular membranes but rather contributes actively in regulating the sorting and trafficking of GPCRs.

The radius of curvature of membrane compartments in living cells typically ranges between 20 nm and 100 nm, making their direct quantitative size determination challenging by diffraction-limited or super-resolution microscopy[12]. However, the integrated fluorescence intensity of a labeled membrane of known geometry can be accurately converted to radius of curvature[13–15]; for example, for vesicles that have a spherical shape the intensity scales with radius squared[16].

Here we exploited this concept to develop a high-throughput strategy for calibrating quantitatively the nanoscopic curvature of individual tubular cell membranes. We used this approach to systematically measure a continuum of cell membrane curvatures, which in turn enabled us to demonstrate for the first time that three class A GPCRs—the neuropeptide Y Y2 receptor (Y2R), the β_1 adrenergic receptor (β_1AR) and the β_2 adrenergic receptor (β_2AR)—were systematically sorted by geometrical membrane curvature in living cells (**Fig. 1** and **Supplementary Results, Supplementary Figs. 1 and 2**). The sorting was modulated to different extents by agonist activation as a result of distinct structural changes within the receptors and ranged from a dramatic redistribution of the Y2R to an insignificant change in the sorting of the β_1AR. Fitting a thermodynamic model revealed that sorting was driven by an energetic drive to match the high intrinsic curvature of the GPCRs ($1/c_p \approx 20$ nm) to the curvature of the membrane.

RESULTS

Initial studies were carried out on the Y2R, a well-characterized class A GPCR, which is involved in cell-shape remodeling events, such as cell migration and angiogenesis[17,18], that require the formation of highly curved membrane protrusions[19]. The Y2R is known to sort into specialized plasma membrane areas such as nerve terminals[20], but how this sorting is realized has not been established. We investigated the sorting of Y2R in neuron-like PC12 cells that have been observed to form a large amount of cell protrusions, the majority of which are filopodia with radii below the diffraction limit[21].

Quantifying Y2R density on filopodia of different radii

To quantify the radius of filopodia by fluorescence microscopy, we labeled the cell membrane with DiOC$_{18}$ (DiO), a lipid dye that is not sorted by tubular membrane curvature[22] (**Fig. 1a,b**). The tubular membrane geometry of filopodia[23,24] allowed us to use the integrated membrane intensity across a diffraction-limited filopodium, I(DiO), as a relative measure of filopodium radius (**Supplementary Fig. 1a,b**). Similarly to published protocols[15,16], we converted the intensity measurement to absolute radius in nanometers by quantifying I(DiO) for a population of pulled cell membrane tethers of known radii (**Supplementary Fig. 1c**). This allowed us to accumulate histograms of accurately determined filopodium radii (**Fig. 1c**), which matched well the reported size range of cell filopodia[8,25]. The wide range of filopodium radii observed in cells probably results from a convolution of membrane-shaping proteins and variable cell

[1]Bionanotechnology and Nanomedicine Laboratory, Nano-Science Center, Department of Chemistry, University of Copenhagen, Copenhagen, Denmark. [2]Lundbeck Foundation Center Biomembranes in Nanomedicine, University of Copenhagen, Copenhagen, Denmark. [3]Niels Bohr Institute, University of Copenhagen, Copenhagen, Denmark. [4]Department of Chemistry, University of Copenhagen, Copenhagen, Denmark. [5]Laboratoire Matière et Systèmes Complexes, Université Paris-Diderot, Paris, France. [6]Present addresses: The Victor Chang Cardiac Research Institute, Sydney, Australia (K.R.R.); Gubra Aps, Hørsholm, Denmark (S.L.P.); Department of Chemistry and Nano-Science Center, University of Copenhagen, Copenhagen, Denmark (N.S.H.). *e-mail: stamou@nano.ku.dk

membrane tension, which among other things is influenced by lipid diffusion barriers and the adhesion between the membrane and the actin cytoskeleton. The high-throughput capacity of the assay enabled us to quantify the radii of thousands of filopodia (**Fig. 1c**), allowing reliable statistical analysis of the data.

To quantify the density of Y2R on filopodia, the PC12 cells were transiently transfected to express the Y2R and seeded on poly-D-lysine–coated glass cover slips for 48 h. The Y2R was N-terminally fused to a SNAP tag[26], allowing its covalent attachment to a water-soluble fluorophore (DY-647) (**Fig. 1a**). The density of Y2R on individual filopodia is proportional to the ratio of the integrated intensities of Y2R and DiO ($\propto I(Y2R)/I(DiO)$) across the filopodium (**Supplementary Fig. 1a,b**). Intensity profiles of the DiO signal and Y2R signal across three filopodia (**Fig. 1d**) showed that as the DiO intensity decreased with filopodium radius, the Y2R to DiO ratio increased (**Fig. 1e**), corresponding to an increased density of Y2R.

Sorting of Y2R scales with membrane curvature

Plotting the normalized density of Y2R as a function of filopodium radius for 61 filopodia within a single cell revealed an exponential-like increase in receptor density in the smallest filopodia, demonstrating that the Y2R is sorted into filopodia of high membrane curvature (**Fig. 1f**). In comparison, two negative controls—aquaporin-0 (AQP0)[27], a member of the major intrinsic proteins, and the membrane dye DiDC$_{18}$ (DiD)—which were both shown in reconstituted systems not to sense membrane curvature (**Supplementary Fig. 2a–c**), did not display any curvature-dependent sorting (**Fig. 1f**). We additionally verified that the membrane dye was not influencing Y2R sorting by measuring curvature-dependent sorting of the receptor in pulled membrane tethers labeled by a cytosolic dye (**Supplementary Fig. 2d–g**).

To confirm that the single-cell phenotype observed was representative of the cell population, we combined hundreds of filopodia measurements from ~30 randomly chosen individual cells. We plotted normalized density as a function of filopodium radius for Y2R (27 cells, 459 filopodia), DiD (32 cells, 442 filopodia) and AQP0 (44 cells, 475 filopodia) (**Fig. 2a–c**). To compare the sorting of Y2R and the two controls we quantified the fold increase in density (F) upon a tenfold decrease in filopodium radius (250 nm to 25 nm) from error-weighted fits to the data sets (**Fig. 2a–c**). The quantification revealed a >3-fold increase in Y2R density in highly curved filopodia ($F = 3.4 \pm 0.3$) relative to DiD ($F = 1.0 \pm 0.2$) and AQP0 ($F = 0.9 \pm 0.2$). The sorting of Y2R in PC12 cells was identical within error to the sorting in HEK293 cells ($F = 3.0 \pm 0.9$), suggesting that Y2R curvature-dependent sorting was not cell-line specific (**Supplementary Fig. 1f** and **Supplementary Table 1**).

Membrane curvature as a causal effector of Y2R sorting

To ensure that the curvature-dependent sorting of Y2R did not rely on specialized actin- or lipid-dependent sorting mechanisms in filopodia[8], we quantified the sorting of the receptor in tethers artificially pulled from random membrane areas of living HEK293 cells (**Fig. 3a**). Tethers were pulled using an optically trapped protein-passivated polystyrene bead. As previously described, the radius of the tethers decreased when they were extended beyond 15 μm owing to depletion of the membrane reservoir[28]. By simultaneous confocal fluorescence imaging of the tether, we could quantify the normalized Y2R density and tether radius as described for the filopodia (**Fig. 3b**). We verified that both receptor and lipid dye were freely diffusing in the tether and had reached equilibrium before imaging (**Supplementary Fig. 3a–d**). Furthermore, by sequential imaging of cells expressing fluorescently labeled F-actin and Y2R, we showed that actin-mediated protein transport[29] was disrupted within the timescale of the Y2R sorting experiment (**Supplementary Fig. 3f**). Histograms of the radius of all examined tethers and filopodia
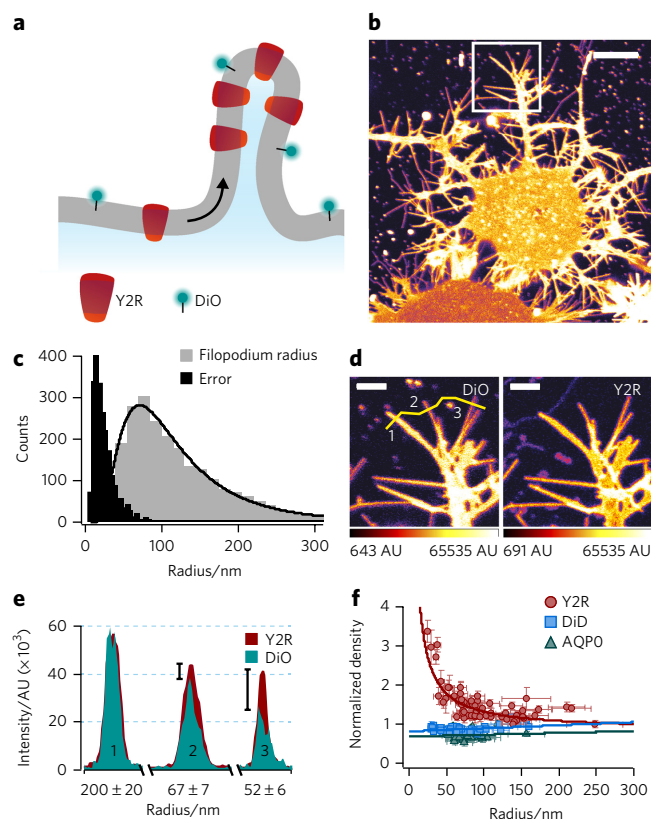
Figure 1 | Quantitative analysis of membrane curvature–dependent sorting of TMPs using live-cell imaging of filopodia. (**a**) Schematic of approach. The Y2R was expressed in PC12 cells and coupled to a water-soluble fluorophore (DY-647). The cellular membrane was labeled with DiO, enabling imaging of receptor and membrane by confocal fluorescence microscopy. (**b**) Micrograph of DiO-labeled PC12 cell filopodia. Scale bar, 10 μm. (**c**) Filopodium radius and error on the size measurement (s.e.m. of three measurements per filopodium) of 2,389 filopodia from 144 cells. (**d**) Zoomed-in view of filopodia (white box in **b**) in the DiO (left) and Y2R (right) channels. Scale bars, 2 μm. Numbers (1–3) indicate three filopodia of decreasing radii. (**e**) Intensity profile (measured as a 5 pixel average along the yellow line in **d**) for DiO (green) and Y2R (red) across 3 filopodia (1–3 in **d**). (**f**) Single-cell measurements of normalized density versus filopodia radius for Y2R ($N_{filopodia} = 61$, red circles), DiD ($N_{filopodia} = 42$, blue squares) and AQP0 ($N_{filopodia} = 33$, green triangles) versus filopodia radius. Error bars, s.e.m. of three intensity measurements on each filopodium. Solid lines are inserted as a guide to the eye.

(**Fig. 3c**) show an ~10-fold lower throughput of pulling tether experiments, owing to the more demanding and time-consuming experimental setup, relative to the filopodia experiments. The normalized Y2R density increased considerably when a single tether was sequentially pulled longer and therefore decreased its radius, demonstrating that the Y2R responds dynamically to changes in membrane curvature (**Fig. 3d**).

Combining tether measurements from multiple cells confirmed that the curvature-dependent sorting of Y2R in tethers ($F = 3.5 \pm 0.2$) was the same as in filopodia ($F = 3.4 \pm 0.3$) (**Fig. 3e**). As observed for the filopodia, neither DiD ($F = 1.0 \pm 0.3$) nor AQP0 ($F = 1.1 \pm 0.1$) showed any curvature-dependent sorting in pulled tethers. Combined plots of the sorting data obtained in HEK293 filopodia, PC12 filopodia and pulled tethers illustrate that the data collapsed to the same master curve (**Supplementary Fig. 1f**), strongly suggesting the presence of a common biophysical sorting mechanism in the three systems.
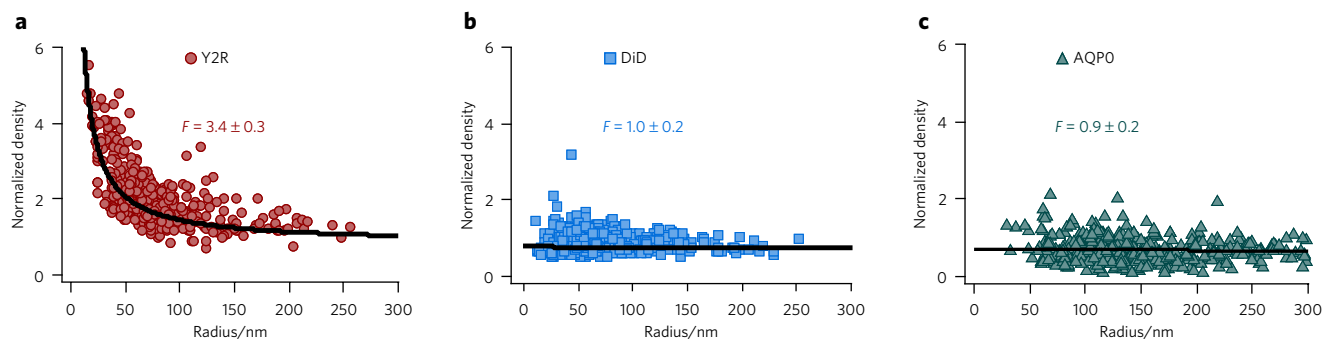
Figure 2 | Combined filopodia measurements from multiple cells verify curvature-dependent sorting of the Y2R. (**a–c**) Normalized density as a function of filopodium radius, combined from N transfections (biological replicates) (**Supplementary Table 1**), displayed for Y2R ($N = 3$, $N_{cells} = 27$, $N_{filopodia} = 459$) (**a**), DiD ($N = 3$, $N_{cells} = 32$, $N_{filopodia} = 442$) (**b**) and AQP0 ($N = 4$, $N_{cells} = 44$, $N_{filopodia} = 475$) (**c**). Fold increase in density, F, between filopodia of 250 nm and 25 nm radius was quantified by fitting a power function (Y2R; Online Methods) or a straight line (DiD and AQP0) to each experiment. F values are mean and s.e.m. of at least three biological replicates (**Supplementary Table 1**).

A thermodynamic model for curvature-mediated sorting

To characterize in depth the molecular mechanisms responsible for the observed sorting, we used a thermodynamic model that was first theoretically outlined in 1981 (ref. 30) and recently refined and validated experimentally for a potassium channel reconstituted in giant unilamellar vesicles[27]. The model is based on the hypothesis that curvature-dependent sorting of TMPs results from an energetic drive to match protein shape and membrane curvature[31–33]. Cell membrane protrusions were modeled as tubular membranes connected to a planar membrane reservoir, and the predicted enrichment of protein results from a balance between the energetic drive to match membrane and protein curvature and the entropic resistance for having different protein densities in the protrusion and membrane reservoir (Online Methods). The parameters controlling curvature-dependent sorting of a protein are its average intrinsic curvature, c_p, which reflects the membrane curvature at which sorting is maximal, and its bending rigidity, κ_p, which energetically penalizes mismatch between membrane and protein curvatures.

Plotting the normalized Y2R density as a function of filopodia curvature ($c = 1/R$) allowed us to perform an error-weighted numerical fit, which revealed the good agreement of the model with the data (**Fig. 4a**). Notably, the model allowed us to estimate quantitatively the intrinsic (or spontaneous) radius of curvature of the Y2R ($1/c_p = 23.3 \pm 0.5$ nm) and its bending rigidity ($\kappa_p = 230 \pm 10$ kJ/mol), which was 1.6-fold the quantified bending rigidity of the cell membrane ($\kappa = (58 \pm 6)\ k_BT \approx 144$ kJ/mol; Online Methods). Our findings

thus suggest the presence of a biophysical mechanism in living cells that enables GPCRs to sort into highly curved membranes that match the intrinsic curvature of the protein. A direct corollary of this hypothesis is that changes in the conformation and, thus, the intrinsic curvature of a receptor should in principle influence its curvature-dependent sorting behavior. We next tested quantitatively this prediction.

Agonists regulate curvature-dependent GPCR sorting

We examined whether inducing a conformational change in the Y2R by agonist activation would change its curvature-dependent sorting. We added the peptide agonist, PYY3-36, at saturation concentration (100 nM)[34] and quantified sorting of the receptor in PC12 cell filopodia after a 5-min incubation. As predicted, plotting the density as a function of curvature revealed a significant change in the sorting of Y2R upon activation (**Fig. 4a**). Numerical fitting of the sorting model to the data enabled us to quantify a ~40% decrease in intrinsic curvature ($\Delta(1/c_p) = 16.0 \pm 0.8$ nm) and a ~200% increase in rigidity ($\Delta\kappa_p = 480 \pm 10$ kJ/mol) of the Y2R upon ligand activation (**Table 1**).

Finally, we investigated whether sorting by membrane curvature was recurrent for two additional members of the class A GPCR family, the β_2AR and the β_1AR. We quantified their sorting in filopodia before and after activation with saturation concentrations (100 µM)[35] of the agonist isoproterenol (ISO) (**Fig. 4b,c**). The extracted structural parameters of the three GPCRs before activation were identical
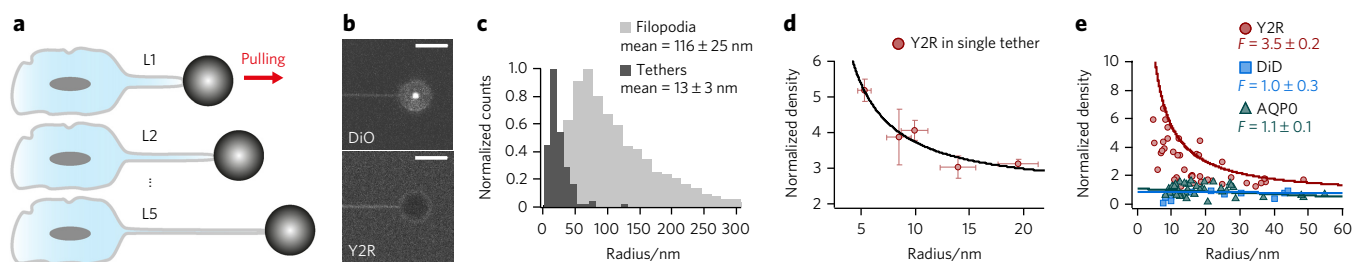

Figure 3 | Membrane curvature–dependent sorting of the Y2R is recurrent in artificially pulled cell membrane tethers. (**a**) Pulling of membrane tethers from random areas of live HEK293 cells. As the tether extends, the radius decreases. (**b**) Micrographs of a pulled tether in the DiO channel (top) and the Y2R channel (bottom). Scale bars, 5 µm. (**c**) Radius histograms of all examined filopodia ($N_{filopodia} = 2,389$, white bars) and pulled tethers ($N_{tethers} = 103$, gray bars). Arithmetic means of the distributions were quantified as described in Online Methods. (**d**) Normalized Y2R density versus tether radius plotted for a single tether successively pulled longer, thereby decreasing its radius. Error bars, s.e.m. of three intensity measurements on each tether. The solid line is inserted as a guide to the eye. (**e**) Combined density measurements of multiple pulled tethers as a function of tether radius for Y2R ($N = 2$, $N_{cells} = 12$, $N_{tethers} = 42$, red), DiD ($N = 1$, $N_{cells} = 5$, $N_{tethers} = 15$, blue) and AQP0 ($N = 2$, $N_{cells} = 11$, $N_{tethers} = 42$, green). Tether data were combined, and $F \pm$ s.d. was quantified as established for filopodia by fitting of a power function (Y2R) or a straight line (DiD and AQP0).
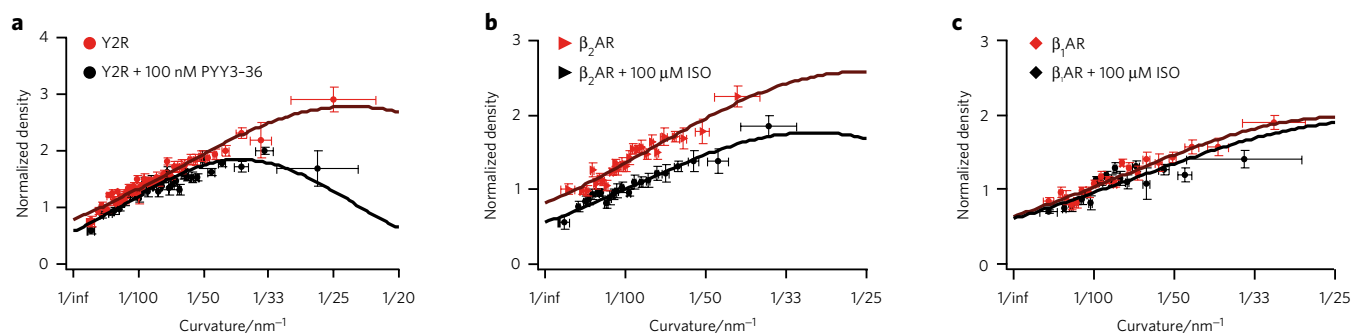
Figure 4 | Curvature-dependent sorting of class A GPCRs is governed by structural properties of the proteins and is regulated by agonist activation.
(**a**–**c**) Normalized Y2R (**a**), β_2AR (**b**) or β_1AR (**c**) density versus filopodium curvature, displayed as error-weighted bins (50 (**a**) or 100 (**b**,**c**) points per bin), together with the numerical fit of the sorting model, before and after agonist activation by PYY3-36 (**a**) or ISO (**b**,**c**). In **a**, $N = 15$, $N_{cells} = 165$, $N_{filopodia} = 2,573$ before activation, and $N = 15$, $N_{cells} = 159$, $N_{filopodia} = 2,013$ after activation; in **b**, $N = 8$, $N_{cells} = 82$, $N_{filopodia} = 1,272$ before activation, and $N = 12$, $N_{cells} = 114$, $N_{filopodia} = 2,240$ after activation; in **c**, $N = 13$, $N_{cells} = 107$, $N_{filopodia} = 1,042$ before activation, and $N = 9$, $N_{cells} = 63$, $N_{filopodia} = 981$ after activation. Error bars, error-weighted s.d. (*x* axis) or error-weighted s.e.m. (*y* axis). All fits were done to the raw data (**Supplementary Fig. 4**) but are displayed together with the binned data to visualize the changes induced by ligand addition. $1/c_p$ and κ_p of the receptors are listed in **Table 1**.

within error (**Table 1**), strongly supporting that sorting by membrane curvature is a generic phenotype that can regulate the spatial localization of class A GPCRs.

We verified that the two ligands used in this work (PYY3-36 and ISO) did not interfere with membrane physical properties by measuring that the average tether force was the same within error for wild-type HEK293 cells before ($f = 28 \pm 5$ pN, $N = 8$) and after addition of 100 nM PYY3-36 ($f = 20 \pm 4$ pN, $N = 8$) or 100 μM ISO ($f = 21 \pm 7$ pN, $N = 8$) (Online Methods).

The three receptors displayed distinct curvature-dependent responses to ligand activation, revealing multiple layers of regulation and specificity encoded in the sorting process. The β_2AR displayed a less pronounced response than the Y2R; i.e., a ~15% decrease in intrinsic curvature ($\Delta(1/c_p) = 5 \pm 3$ nm) and a ~40% increase in rigidity ($\Delta\kappa_p = 90 \pm 50$ kJ/mol). However, the β_1AR, though incubated with the same ligand as the β_2AR, did not show a significant change in its sorting behavior upon ligand binding. The latter observation prompted us to hypothesize that the degree of receptor contraction and stabilization may be correlated to the strength of the ligand-receptor binding. Indeed, in support of this proposition, we observed a correlation between the Gibbs free energy of ligand binding, ΔG, and the quantified structural changes, $\Delta(1/c_p)$ and $\Delta\kappa_p$, for all three ligand-receptor pairs (**Supplementary Fig. 4f**).

To account for sorting not mediated by membrane curvature, we also included a protein interaction term in the model: $\Delta\alpha = \alpha_c - \alpha_f$, which represents the energetic difference between protein–protein interactions taking place on the filopodia (α_f) and on the cell body (α_c). The sign of $\Delta\alpha$ reflects more ($\Delta\alpha > 0$) or less ($\Delta\alpha < 0$) attractive interactions in the cell body plasma membrane (Online Methods). For all tested receptors, we found $\Delta\alpha > 0$ (0.2–0.5 $k_B T/nm^2$, with relative errors ranging from 2% to 10%), resulting in a normalized density <1 at $c = 0$ (**Fig. 4**), suggesting that protein–protein

interactions are more attractive on the cell body plasma membrane than on the filopodium. In addition, we observed for all receptors an increase in $\Delta\alpha$ (ranging from 10% to 170%) upon ligand binding, in agreement with an increase in protein interactions with, for example, adaptor proteins on the cell body plasma membrane upon activation.

DISCUSSION

It has long been hypothesized that TMPs such as GPCRs can partition into their sites of action by recognizing the curvature of the membrane[31,32,36]. However, to date there have been only a few examples of live-cell measurements that investigate membrane curvature–dependent protein sorting[37–39]. These assays have focused primarily on peripheral membrane proteins and have provided qualitative answers to whether a protein is localized in areas of expected high curvature. By establishing a direct quantitative correlation between membrane curvature and protein density, the strategy presented here provides unprecedented insight into the molecular mechanism by which membrane curvature can regulate the sorting of TMPs within curved cellular membranes.

The crystal structures of class A GPCRs[40,41] have revealed that their highly homologous transmembrane segment[42] is asymmetrical across the bilayer[43] (**Supplementary Fig. 4d**). This suggests a nonzero intrinsic curvature, which is in general agreement with our findings (though the intrinsic curvature cannot be quantitatively predicted from the crystal structure of a protein)[27]. In addition, our findings are in agreement with molecular dynamics simulations that have estimated the spontaneous curvature of the bilayer surrounding the prototypical class A GPCR rhodopsin to be overall positive (~1/100 nm⁻¹)[43] and revealed that the highly curved geometry of the cubic bilayer phase provides the most efficient shielding of the protein from unfavorable hydrophobic exposure[44]. The curvature-driven sorting we observe in continuous membranes of living cells is also in line with measurements of the β_2AR reconstituted in proteoliposomes, which revealed a higher protein–lipid ratio in liposomes of higher membrane curvature[45], again pointing to a nonzero intrinsic protein curvature.

In agreement with previous findings[27], we observed no curvature-mediated sorting of AQP0. These results are consistent with the crystal structure of the AQP0 tetramer, which reveals a uniform, cylindrical shape ($c_p = 0$)[46], and they suggest that the rigidity is not high enough ($\kappa_p/\kappa \approx 1$) for AQP0 to measurably couple its density to membrane curvature.

The quantified structural changes in response to ligand activation are in qualitative agreement with current knowledge on the activation

Table 1 | Extracted fitting parameters for Y2R, β_2AR and β_1AR

	Before activation		Activation		
	$1/c_p$ (nm)	κ_p (kJ/mol)	Agonist	$\Delta(1/c_p)$ (nm)	$\Delta\kappa_p$ (kJ/mol)
Y2R	23.3 ± 0.5	230 ± 10	100 nM PYY3-36	16.0 ± 0.8	480 ± 10
β_2AR	26 ± 3	250 ± 40	100 μM ISO	5 ± 3	90 ± 50
β_1AR	24 ± 1	220 ± 23	100 μM ISO	-2 ± 2	-30 ± 30

Extracted intrinsic curvature ($1/c_p$) and bending rigidity (κ_p) of the receptors before and after activation with the indicated agonists. The error on the fitting parameters is the extracted standard error (Online Methods).

of class A GPCRs. Ligand binding has been reported to induce, on average, a small contraction in the extracellular part and a larger expansion of the intracellular part of the protein[41,47,48], in agreement with a decrease in c_p (**Supplementary Fig. 4e**). The quantified increase in κ_p might seem contradictory to recent findings showing that agonist binding to GPCRs can increase the conformational dynamics of the intracellular part of the protein[48]. However, agonist binding has also been shown to induce contraction and stabilization and thus, probably, a stiffening of the extracellular part of the protein, which contains the ligand binding pocket[47,48]. The extracted κ_p in this study represents an average rigidity for the whole protein and suggests that, even if parts of the protein become more dynamic, the overall rigidity is increasing.

Here we demonstrate a previously unknown mechanism for sorting GPCRs that is directly relevant for sorting processes occurring in highly curved tubular architectures emanating from cells, such as filopodia and microvilli[8], and in intracellular sorting compartments, such as the endoplasmic reticulum and endosome tubules[9,10]. It is plausible that membrane curvature is involved both in ensuring the efficient interaction with adaptor proteins upon GPCR activation[3] and in the subsequent trafficking and recycling of the receptors[10]. As ligand binding can regulate the coupling between membrane curvature and GPCR structure, we would predict that membrane curvature should, conversely, be able to modulate the structure and conformational landscape of GPCRs. Our findings therefore also suggest a role for cellular membrane curvature as a regulator of GPCR function and as such have wide implications for receptor-based cell signaling.

More broadly, our data reveal that the biomechanical coupling between the shape and rigidity of a TMP and membrane morphology is strong enough to regulate TMP distribution in competition with the plethora of sorting processes mediated by protein–protein[3,49] and protein–lipid[36,50] interactions that ultimately define the behavior of living cells. This sorting mechanism thus becomes relevant for TMPs in general and is likely to affect biological processes, such as endo- and exocytosis, that involve other curvature types (for example, spherical, positive, negative or hyperbolic). We envision that quantitative live-cell strategies such as the one presented here will be instrumental in fully elucidating the contribution of membrane curvature to the multitude of sorting and activation mechanisms in the cell[11].

METHODS

Methods, including statements of data availability and any associated accession codes and references, are available in the online version of the paper.

References

1. Allen, J.A., Halverson-Tamboli, R.A. & Rasenick, M.M. Lipid raft microdomains and neurotransmitter signalling. *Nat. Rev. Neurosci.* **8**, 128–140 (2007).
2. Irannejad, R. *et al.* Conformational biosensors reveal GPCR signalling from endosomes. *Nature* **495**, 534–538 (2013).
3. Ritter, S.L. & Hall, R.A. Fine-tuning of GPCR activity by receptor-interacting proteins. *Nat. Rev. Mol. Cell Biol.* **10**, 819–830 (2009).
4. Soubias, O., Teague, W.E. Jr., Hines, K.G. & Gawrisch, K. Rhodopsin/lipid hydrophobic matching-rhodopsin oligomerization and function. *Biophys. J.* **108**, 1125–1132 (2015).
5. Kimura, T. *et al.* Recombinant cannabinoid type 2 receptor in liposome model activates G protein in response to anionic lipid constituents. *J. Biol. Chem.* **287**, 4076–4087 (2012).
6. Mondal, S. *et al.* Membrane driven spatial organization of GPCRs. *Sci. Rep.* **3**, 2909 (2013).
7. Koldsø, H. & Sansom, M.S. Organization and Dynamics of Receptor Proteins in a Plasma Membrane. *J. Am. Chem. Soc.* **137**, 14694–14704 (2015).
8. Mattila, P.K. & Lappalainen, P. Filopodia: molecular architecture and cellular functions. *Nat. Rev. Mol. Cell Biol.* **9**, 446–454 (2008).
9. Zimmerberg, J. & Kozlov, M.M. How proteins produce cellular membrane curvature. *Nat. Rev. Mol. Cell Biol.* **7**, 9–19 (2006).
10. Temkin, P. *et al.* SNX27 mediates retromer tubule entry and endosome-to-plasma membrane trafficking of signalling receptors. *Nat. Cell Biol.* **13**, 715–721 (2011).
11. Iversen, L., Mathiasen, S., Larsen, J.B. & Stamou, D. Membrane curvature bends the laws of physics and chemistry. *Nat. Chem. Biol.* **11**, 822–825 (2015).
12. Shim, S.H. *et al.* Super-resolution fluorescence imaging of organelles in live cells with photoswitchable membrane probes. *Proc. Natl. Acad. Sci. USA* **109**, 13978–13983 (2012).
13. Veshaguri, S. *et al.* Direct observation of proton pumping by a eukaryotic P-type ATPase. *Science* **351**, 1469–1473 (2016).
14. Sorre, B. *et al.* Nature of curvature coupling of amphiphysin with membranes depends on its bound density. *Proc. Natl. Acad. Sci. USA* **109**, 173–178 (2012).
15. Larsen, J.B. *et al.* Membrane curvature enables N-Ras lipid anchor sorting to liquid-ordered membrane phases. *Nat. Chem. Biol.* **11**, 192–194 (2015).
16. Kunding, A.H., Mortensen, M.W., Christensen, S.M. & Stamou, D. A fluorescence-based technique to construct size distributions from single-object measurements: application to the extrusion of lipid vesicles. *Biophys. J.* **95**, 1176–1188 (2008).
17. Kuo, L.E. *et al.* Neuropeptide Y acts directly in the periphery on fat tissue and mediates stress-induced obesity and metabolic syndrome. *Nat. Med.* **13**, 803–811 (2007).
18. Movafagh, S., Hobson, J.P., Spiegel, S., Kleinman, H.K. & Zukowska, Z. Neuropeptide Y induces migration, proliferation, and tube formation of endothelial cells bimodally via Y1, Y2, and Y5 receptors. *FASEB J.* **20**, 1924–1926 (2006).
19. Gerhardt, H. *et al.* VEGF guides angiogenic sprouting utilizing endothelial tip cell filopodia. *J. Cell Biol.* **161**, 1163–1177 (2003).
20. Stanić, D. *et al.* Characterization of neuropeptide Y2 receptor protein expression in the mouse brain. I. Distribution in cell bodies and nerve terminals. *J. Comp. Neurol.* **499**, 357–390 (2006).
21. Rustom, A., Saffrich, R., Markovic, I., Walther, P. & Gerdes, H.H. Nanotubular highways for intercellular organelle transport. *Science* **303**, 1007–1010 (2004).
22. Tian, A. & Baumgart, T. Sorting of lipids and proteins in membrane curvature gradients. *Biophys. J.* **96**, 2676–2688 (2009).
23. Bornschlögl, T. *et al.* Filopodial retraction force is generated by cortical actin dynamics and controlled by reversible tethering at the tip. *Proc. Natl. Acad. Sci. USA* **110**, 18928–18933 (2013).
24. Romero, S. *et al.* Filopodium retraction is controlled by adhesion to its tip. *J. Cell Sci.* **125**, 4999–5004 (2012).
25. Revenu, C., Athman, R., Robine, S. & Louvard, D. The co-workers of actin filaments: from cell structures to signals. *Nat. Rev. Mol. Cell Biol.* **5**, 635–646 (2004).
26. Keppler, A. *et al.* A general method for the covalent labeling of fusion proteins with small molecules *in vivo*. *Nat. Biotechnol.* **21**, 86–89 (2003).
27. Aimon, S. *et al.* Membrane shape modulates transmembrane protein distribution. *Dev. Cell* **28**, 212–218 (2014).
28. Brownell, W.E., Qian, F. & Anvari, B. Cell membrane tethers generate mechanical force in response to electrical stimulation. *Biophys. J.* **99**, 845–852 (2010).
29. Leijnse, N., Oddershede, L.B. & Bendix, P.M. Helical buckling of actin inside filopodia generates traction. *Proc. Natl. Acad. Sci. USA* **112**, 136–141 (2015).
30. Markin, V.S. Lateral organization of membranes and cell shapes. *Biophys. J.* **36**, 1–19 (1981).
31. Ramaswamy, S., Toner, J. & Prost, J. Nonequilibrium fluctuations, traveling waves, and instabilities in active membranes. *Phys. Rev. Lett.* **84**, 3494–3497 (2000).
32. Netz, R.R. & Pincus, P. Inhomogeneous fluid membranes: Segregation, ordering, and effective rigidity. *Phys. Rev. E Stat. Phys. Plasmas Fluids Relat. Interdiscip. Topics* **52**, 4114–4128 (1995).
33. Božič, B., Kralj-Iglič, V. & Svetina, S. Coupling between vesicle shape and lateral distribution of mobile membrane inclusions. *Phys. Rev. E* **73**, 041915 (2006).
34. Keire, D.A. *et al.* Primary structures of PYY, [Pro^{34}]PYY, and PYY-(3-36) confer different conformations and receptor selectivity. *Am. J. Physiol. Gastrointest. Liver Physiol.* **279**, G126–G131 (2000).
35. Baker, J.G. The selectivity of β-adrenoceptor agonists at human β1-, β2- and β3-adrenoceptors. *Br. J. Pharmacol.* **160**, 1048–1061 (2010).
36. Lippincott-Schwartz, J. & Phair, R.D. Lipids and cholesterol as regulators of traffic in the endomembrane system. *Annu. Rev. Biophys.* **39**, 559–578 (2010).
37. Ramamurthi, K.S., Lecuyer, S., Stone, H.A. & Losick, R. Geometric cue for protein localization in a bacterium. *Science* **323**, 1354–1357 (2009).
38. Galic, M. *et al.* External push and internal pull forces recruit curvature-sensing N-BAR domain proteins to the plasma membrane. *Nat. Cell Biol.* **14**, 874–881 (2012).

39. Hägerstrand, H. *et al.* Curvature-dependent lateral distribution of raft markers in the human erythrocyte membrane. *Mol. Membr. Biol.* **23**, 277–288 (2006).

40. Palczewski, K. *et al.* Crystal structure of rhodopsin: a Gprotein-coupled receptor. *Science* **289**, 739–745 (2000).

41. Rasmussen, S.G.F. *et al.* Structure of a nanobody-stabilized active state of the β_2 adrenoceptor. *Nature* **469**, 175–180 (2011).

42. Costanzi, S. On the applicability of GPCR homology models to computer-aided drug discovery: a comparison between *in silico* and crystal structures of the β2-adrenergic receptor. *J. Med. Chem.* **51**, 2907–2914 (2008).

43. Huber, T., Botelho, A.V., Beyer, K. & Brown, M.F. Membrane model for the G-protein-coupled receptor rhodopsin: hydrophobic interface and dynamical structure. *Biophys. J.* **86**, 2078–2100 (2004).

44. Khelashvili, G. *et al.* Why GPCRs behave differently in cubic and lamellar lipidic mesophases. *J. Am. Chem. Soc.* **134**, 15858–15868 (2012).

45. Mathiasen, S. *et al.* Nanoscale high-content analysis using compositional heterogeneities of single proteoliposomes. *Nat. Methods* **11**, 931–934 (2014).

46. Gonen, T., Sliz, P., Kistler, J., Cheng, Y. & Walz, T. Aquaporin-0 membrane junctions reveal the structure of a closed water pore. *Nature* **429**, 193–197 (2004).

47. Warne, T. *et al.* Structure of a β1-adrenergic G-protein-coupled receptor. *Nature* **454**, 486–491 (2008).

48. Nygaard, R. *et al.* The dynamic process of β_2-adrenergic receptor activation. *Cell* **152**, 532–542 (2013).

49. Salaita, K. *et al.* Restriction of receptor movement alters cellular response: physical force sensing by EphA2. *Science* **327**, 1380–1385 (2010).

50. Sharpe, H.J., Stevens, T.J. & Munro, S. A comprehensive comparison of transmembrane domains reveals organelle-specific properties. *Cell* **142**, 158–169 (2010).

Author contributions

D.S. designed and supervised the project. K.R.R. conducted all experiments and data analysis, A.M. assisted with experiments and data analysis, V.T. helped with cell culturing, and N.S.H. helped design experiments and discuss results. A.C.-J. developed the theoretical sorting model and performed the numerical fits. L.B.O. provided the optical tweezers setup and supervised the optical trapping experiments. N.L. and K.R.R. conducted the pulling tether experiments. N.L. provided the expertise in using the laser tweezers setup, and P.M.B. discussed results and data treatment. K.L.M. and V.F.W. provided the plasmid and know-how for expressing the SNAP-tagged Y2R, β_1AR and β_2AR. K.J.J. and S.L.P. synthesized the PYY3-36 peptide. All authors discussed the results and commented on the manuscript, which was written by K.R.R. and D.S.

Competing financial interests

The authors declare no competing financial interests.

Additional information

Any supplementary information, chemical compound information and source data are available in the online version of the paper. Reprints and permissions information is available online at http://www.nature.com/reprints/index.html. Publisher's note: Springer Nature remains neutral with regard to jurisdictional claims in published maps and institutional affiliations. Correspondence and requests for materials should be addressed to D.S.

ONLINE METHODS

Materials. For fluorescent labeling, 3,3′-dioctadecyloxacarbocyanine perchlorate ($DiOC_{18}$ (DiO)) (purity ≥ 95% at 490 nm) and 1,1′-dioctadecyl-3,3,3′,3′-tetramethylindodicarbocyanine 4-chlorobenzenesulfonate salt ($DiDC_{18}$ (DiD, ≥ 95% at 644 nm)) were purchased at Invitrogen Life Technologies. SNAP-Surface647 (SNAP647) (purity ≥ 99%) was purchased from New England BioLabs. For cell culture, PC12 cells (ATCC CRL-1721) and HEK293 cells (ATCC CRL-1573) were purchased from ATCC. DMEM (41966-029), RPMI 1640 (11835-063), horse serum (HS) (26050-070), FBS (10082-139), penicillin–streptomycin (Pen/Strep) (15140-148), sodium pyruvate (SP) (11360-039), geneticin (10131-019), 0.05% trypsin-EDTA (25300-054), DPBS (without $CaCl_2$ or $MgCl_2$) and DPBS (with $CaCl_2$ and $MgCl_2$) were purchased from Invitrogen Life Technologies. TurboFect transfection reagent was purchased from Thermo Scientific, and OptiMem (31985-070) was purchased from Invitrogen Life Technologies. Effectene transfection reagent was purchased at Qiagen. Cytochalasin D (C8273), poly-D-lysine hydrobromide (PDL) and (−)–ISO (I2760, purity ≥ 98%) were purchased from Sigma-Aldrich. Streptavidin-coated microspheres (d = 4.95 μm) were purchased from Bangs Laboratories Inc. 18-mm cover slips (t = 0.17 ± 0.01 mm) were purchased from VWR. 24 × 50 mm cover slips (#1 or #1.5) and 18 × 18 mm cover slips (#1 0.13–0.16 mm) were purchased from Menzel-Gläser.

Peptide synthesis. PYY3-36 was synthesized as described[51]. Briefly, the peptide was prepared by Fmoc-SPPS on TentaGel Rink Amide resin. N^α-Fmoc amino acids (4.0 equiv.) were coupled using HBTU (3.8 equiv.), hydroxybenzotriazole (HOBt, 3.6 equiv.), 1-hydroxy-7-azabenzotriazole (HOAt, 0.4 equiv.) and N,N-diisopropylethylamine (DIEA, 7.8 equiv.) as coupling reagents in dimethylformamide (DMF) for 2 × 2 h. N^α-deprotection was performed using piperidine-DMF (2:3) for 3 min, followed by piperidine-DMF (1:4) for 10 min and finally for 17 min. After treating the peptidyl-resin with TFA–TES–H_2O (95:2:3) for 2 h, the peptide was precipitated with diethyl ether. The peptide was purified by preparative RP-HPLC to a purity of >95% determined by UV (**Supplementary Fig. 5**). The calculated mass for $C_{180}H_{279}N_{53}O_{54}$ is 4,049.5 Da; the experimental mass was 810.2 Da $(M+5H)^{5+}$ and 1,012.8 Da $(M+6H)^{6+}$.

Plasmid constructs. We purchased the plasmid for SNAP-tagged neuropeptide Y receptor 2 (Y2R-SNAP) from Cisbio Bioassays (France). Plasmids for SNAP-tagged β_1AR and β_2AR receptors (β_1AR-SNAP and β_2AR-SNAP) were obtained from Covalys (Switzerland). cDNA encoding human AQP0 (BC117474) was purchased from Open Biosystems, Thermo Scientific. The full-length Aqp0 fusion with C-terminal mKate2 was obtained by subcloning a XhoI-HindIII PCR-amplified gene into the same sites of pmKate2-N (Evrogen). DNA sequencing was used to verify the sequence.

Cell culturing. PC12 cells were cultured in RPMI-1640 medium supplemented with 10% HS, 5% FBS, 1% SP (final concentration: 1 mM) and 1% Pen/Strep (final concentration: 100 units/mL). HEK293 cells were cultured in DMEM supplemented with 10% FBS and 1% Pen/Strep (final concentration: 100 units/mL). Both cell lines were grown in a 5% CO_2 atmosphere with 100% relative humidity in an incubator at 37 °C. The cell lines were authenticated as recommended by ATCC by morphology inspection using microscopy and growth curve analysis. The PC12 cell line was additionally authenticated by (i) induction of neurite outgrowth by addition of nerve growth factor, (ii) presence of secretory vesicles containing typical protein markers such as synaptophysin and neuropeptide Y, which were secreted upon stimulation, and (iii) the presence of Thy-1 antigen on the cell surface. The cell lines were tested routinely for mycoplasma using Hoechst 33258. The HEK293 cell line is on the list of frequently misidentified or cross-contaminated cell lines. However, to our knowledge, no PC12 cell contamination has been reported in HEK293 cells, and thus in this study they serve the purpose as a control non-neuronal cell line to ensure that the observed sorting is not specific for PC12 cells.

Cell transfection, labeling and activation. For the filopodia assay, cells were transfected in 6-well plates after growing for 24 h on cover slips to ~50% confluency. The medium was exchanged with fresh medium (900 μL per well) and a solution of plasmid, Turbofect and OptiMEM (1 μg: 2 μL: 100 μL per well)

were added after 20 min incubation. Cells were incubated for 24 h before imaging. For the pulling-tether assay, cells were transfected in T25 culture flasks 24 h before attachment on cover slips. Buffer, plasmid and enhancer (75 μL, 0.6 μL and 2.4 μL, respectively) were mixed and incubated for 2–5 min before addition of Effectene (6 μL). After 5–10 min incubation the solution was added together with 2.5 μL growth medium, and the cells were incubated for 4 h before medium was exchanged. The cells were imaged 48–72 h after transfection. For both assays, labeling was done before imaging in the microscope chambers. SNAP647 (1 mM in DMSO) was diluted 200× (5 μM end concentration) in growth medium and added to the cells. After incubation for 10 min at room temperature, the cells were washed three times in imaging medium (filopodia assay) or DPBS (pulling-tether assay). DiO (1 mM in DMSO) was diluted 500× in imaging medium or DPBS and added (2 μM end concentration) to the cells. After 10 min incubation the cells were washed three times in imaging medium or DPBS. For the Y2R we added peptide agonist PYY3-36 (100 nM) to PC12 cells expressing SNAP-labeled Y2R. For the β_1AR and β_2AR we added agonist ISO (100 μM) to PC12 cells expressing SNAP-labeled β_1AR and β_2AR, respectively. As ISO is known to hydrolyze it was kept under vacuum until usage. For both receptors agonist was added 5 min before measuring.

Filopodia assay. Cells (200,000–300,000 per well, ~1.7 mL) were transferred to microscope cover slips (18 mm, round) in a 6-well plate. Prior to cell attachment, the cover slips were incubated at room temperature for 2 h with PDL (0.1 mg/mL in sterile Milli-Q water (MQ)) and subsequently washed three times—first in 2 mL MQ, then in 2 mL PBS and finally in 2 mL medium. The cells were transiently transfected after 24 h and imaged after 48 h. The cell membrane and protein were labeled before imaging as described above. Cells labeled with both membrane and protein dye were examined with a Leica TCS SP5 inverted confocal microscope using a water immersion objective HC PL APO CS ×63 (NA 1.2). Detection of the cell membrane labeled by DiO was performed at 495–580 nm (excitation 488 nm); detection of DiD or SNAP647-labeled proteins was performed at 640–750 nm (excitation 633 nm); detection of mKate2-labeled proteins was performed at 600–700 nm (excitation 594 nm). In all cases, sequential imaging was used to avoid cross-excitation. Images had a resolution of 2,048 × 2,048 pixels, with a pixel size of 44.5 nm and a bit depth of 16. A sample size of 8–16 cells (corresponding to 59–267 filopodia) per experiment produced reproducible results between individual experiments (**Supplementary Table 1**) while making it feasible to image all cells within 40 min of labeling. Focusing the confocal imaging plane on the cover slip surface enabled us to measure exclusively on filopodia adhered to the surface. Filopodia that were closer together than the diffraction limit typically differed either in length or in the direction of propagation. Filopodia that were out of focus or positioned too close to each other were excluded from the analysis by manual inspection.

Pulling-tether assay. Cells (48–72 h after transfection) were transferred to cover slips (24 × 50 mm) and cultured for 2–4 h. Closed chambers were prepared by addition of two stripes of vacuum grease to the cover slip and pressing a small cover slip (18 × 18 mm) tightly on top. The chamber was then filled with a solution of beads (streptavidin-coated microspheres) diluted to 0.02% in DPBS (with $CaCl_2$ and $MgCl_2$), and the chamber was sealed off with vacuum grease. The cell membrane and protein were labeled before sealing. The cells were examined with a Leica TCS SP5 inverted confocal microscope equipped with a water immersion objective HCX PL APO CS ×63 (NA 1.2). The tightly focused trapping laser was coupled into the back port of the microscope and focused through the objective with the correction collar set to 0.14 to optimize trapping for the relevant thickness of the cover glass[52]. A bead was trapped using a laser power of ~500 mW, and the sample was manually translated with a piezo stage to bring the bead in contact with a cell for <1 s. A membrane tether was formed by carefully translating the cell on the stage ~10 μm away from the trapped bead. The height of the trapped bead was adjusted, using a telescope lens[53], such that the tether was in focus of the confocal imaging plane. The same tether was elongated up to five times by translating the piezo stage, and images were acquired after each elongation. The excitation and detection wavelengths were the same as for the filopodia assay. In all cases, sequential imaging was used to avoid cross-excitation and images had a resolution of 1,024 × 1,024 pixels.

Owing to the more demanding and time-consuming experimental setup, as compared to the filopodia experiments, we had a lower throughput of pulling-tether experiments. A sample size of 5–13 cells (corresponding to 15–42 tethers) per experiment reproduced the results quantified in filopodia.

Data treatment. Image analysis and data treatment were performed using custom scripts (available on request) in Igor Pro (Wavemetrics) and Fiji (ImageJ).

Quantification of protein density in single tubular membrane protrusions. The integrated DiO intensity across a filopodium, $I(\text{DiO})_f$, is theoretically predicted to scale linearly with filopodium radius (R_{filo}):

$$I(\text{DiO})_f \propto N_{\text{fluorophores}} \propto A_{\text{surface}} \propto R_{\text{filo}}$$

where A_{surface} is the surface area of the diffraction limited filopodium. Thus, the density of Y2R on a filopodium is proportional to the ratio between the integrated intensities, I_f, of the protein and the membrane dye:

$$\text{Density} \propto I(\text{Y2R})_f / I(\text{DiO})_f$$

The fact that the quantification relies on ratio imaging between protein labels and membrane dyes makes the assay robust against focal drift, as the laser foci are aligned to be at the same height for all lasers and therefore both dyes will be affected similarly if the filopodium is slightly out of focus. Micrographs of filopodia and a zoom in on an individual filopodium in the DiO (green) and Y2R (red) channel are displayed in **Supplementary Figure 1a** together with corresponding intensity profiles across a single filopodium. To compare data from different cells, we normalized to the cell–cell variation in Y2R transfection level and DiO labeling efficiency. This was accomplished by quantifying the integrated intensities of Y2R and DiO across the plasma membrane, I_{PM}, in the middle of the cell (**Supplementary Fig. 1b**). Because the confocal optical section thickness (~0.5 µm) is much smaller than the thickness of the cells (~10–20 µm), the plasma membrane within the optical section (when focused in the middle of the cell) is, to a good approximation, oriented perpendicular to the imaging plane. Under the assumption that the total portion of sub-resolution sized folds is similar for different cells, the plasma membrane area within the confocal volume should therefore be the same. The resulting relative filopodia radius, $I(\text{DiO})$, and normalized Y2R density were quantified as the intensity ratios:

$$I(\text{DiO}) = I(\text{DiO})_f / I(\text{DiO})_{\text{PM}}$$

$$\text{Norm density} = \frac{I(\text{Y2R})_f / I(\text{DiO})_f}{I(\text{Y2R})_{\text{PM}} / I(\text{DiO})_{\text{PM}}}$$

The integrated intensities were extracted by fitting Gaussian functions to the intensity profiles and the final intensity measurement corresponds to the average of three independent measurements on each filopodium. The corresponding errors were propagated from the s.e.m. of the three measurements.

To establish the conversion factor between $I(\text{DiO})$ and the known physical radius of short cell membrane tethers[54], we pulled short (<15 µm) cell membrane tethers from living DiO-labeled HEK293 cells using an optically trapped streptavidin-coated bead, as described above. Imaging by confocal fluorescence microscopy allowed us to quantify $I(\text{DiO})$ for 25 individual tethers. The extracted $I(\text{DiO})$ values were plotted in a histogram that was fitted with a Gaussian function to extract the mean of the population (**Supplementary Fig. 1c**). The mean radius, R, of short (<15 µm) 3T3 cell membrane tethers was previously quantified by scanning electron microscopy as $R = 49 \pm 4$ nm (ref. 54). Relating the mean $I(\text{DiO})$ value to the published tether radius provided a conversion factor, $C = R/I(\text{DiO})$, which was subsequently used to convert $I(\text{DiO})$ to filopodia radius.

To determine the accuracy of the measurements, we fitted the density and radius histograms, as well as their corresponding errors, by a lognormal function to extract the location parameter, μ, and scale parameter, σ, from which the arithmetic mean and s.d. were calculated:

$$\text{mean} = e^{\mu + 0.5\sigma^2}$$

$$\text{s.d.} = e^{\mu + 0.5\sigma^2}\sqrt{e^{\sigma^2} - 1}$$

For all examined proteins or lipid dyes the majority of the errors were within 2% and 20% of the corresponding measurement (**Supplementary Fig. 1e**).

Quantification of tether radius and protein density using a cytosolic dye. We quantified the curvature-dependent sorting of Y2R in pulled tethers, using calcein-AM (calcein) labeling of the cytosol for quantifying tether size (**Supplementary Fig. 2d,e**). As calcein labels the lumen of the tether, the integrated calcein intensity across the tether $I(\text{Cal})_f$ under the assumption of no actin in the tether (**Supplementary Fig. 3f**) is proportional to R^2 where R is the radius of the tether. Thus, the square root of the integrated intensity is theoretically predicted to scale linearly with R, which again scales linearly with the surface area of the tether, A_{surface}:

$$\sqrt{I(\text{Cal})_f} \propto R \propto A_{\text{surface}}$$

Using similar arguments as for the membrane dye, we can quantify the relative tether size, $I(\text{Cal})$, and normalized Y2R density by normalizing to the calcein intensity measured in the cytosol in the middle of the cell, $I(\text{Cal})_C$:

$$I(\text{Cal}) = \sqrt{I(\text{Cal})_f} / \sqrt{I(\text{Cal})_C}$$

$$\text{Norm density} = \frac{I(\text{Y2R})_f / \sqrt{I(\text{Cal})_f}}{I(\text{Y2R})_{\text{PM}} / \sqrt{I(\text{Cal})_C}}$$

Fluorescence recovery after photobleaching (FRAP). To ensure that Y2R and DiO were freely diffusing in the pulled tether we bleached the tether close to the bead (in both channels) and measured the fluorescence recovery as a function of time (**Supplementary Fig. 3**). By normalizing the recovery curve and fitting an exponential function we could extract the recovery time constant, τ, and calculate the half-life of recovery, $t_{1/2}$. By ascribing the entire delay in fluorescence recovery to the tether surface, the minimum diffusion constant ($D_{T,\text{min}}$) was calculated as[55]

$$D_{T,\text{min}} = \frac{4}{\pi^2}\frac{L^2}{\tau}$$

where L is the length of the bleached part of the tether. Both Y2R and DiO recovered fully upon bleaching, confirming that they were freely diffusing in the tether (**Supplementary Fig. 3b,c**). The minimum diffusion constant and half-life of recovery were quantified by averaging three FRAP measurements.

Quantification of the fold increase in density (F). To compare the sorting of Y2R and the two controls we quantified F upon a tenfold decrease in filopodia radius (from 250 nm to 25 nm). The normalized density (S) of a curvature-sensing TMP as a function of filopodia radius (R) can be approximated by a shifted power law, $S = S_0 + B/R$, where B is a constant and S_0 is the sorting limit as the tube curvature is extrapolated to 0 ($R \rightarrow \infty$) (see the TMP sorting model below), whereas the density of the two controls displayed a linear dependency with filopodium radius. Thus, we quantified F from the error-weighted fit of a power function (Y2R) or a straight line (DiD and AQP0) to the data sets (**Fig. 2a–c**). The resulting F values are an average of at least three individual experiments (**Supplementary Table 1**).

The TMP sorting model. We present the thermodynamic model of transmembrane protein (TMP) sorting used to fit the experimental data. We first write down the membrane free energy in the presence of TMPs. We then calculate the enrichment of protein on a tubular membrane (for example, filopodium) relative to the plasma membrane of the cell body, referred to as the normalized density S.

Energy of a membrane with TMPs. In the presence of TMPs, the membrane free energy consists of three terms:

1. Phospholipid membrane bending energy. Assuming constant mean curvature, H, and neglecting spontaneous curvature this bending energy density (per unit area) is given by

$$f_b = \frac{\kappa}{2}(2H)^2 \tag{1}$$

In this equation, κ is the membrane bending rigidity and H is the mean curvature of the cell body plasma membrane or of the tubular membrane (filopodium or pulled tether). For the cell body plasma membrane, the average curvature is 0, and thus we assume $H = 0$. For the tubular membrane, $H = 1/(2R)$, R being the tube radius.

2. Protein–membrane curvature mismatch. Mismatch between the protein and membrane curvatures costs energy, given by the expression[56]

$$f_{\mathrm{mismatch}} = \frac{1}{2}\kappa_{\mathrm{p}}\phi(2H - c_{\mathrm{p}})^2 \tag{2}$$

A similar description of protein–membrane interaction has previously been described elsewhere[27]. In equation (2) $\kappa_{\mathrm{p}} > 0$ is a stiffness constant, reflecting, at the coarse-grained level, the bending rigidity of a protein-membrane patch. Also, c_{p} is the protein's intrinsic curvature, as observed on the mesoscopic scale. Here ϕ refers to the protein area fraction, either on the cell body plasma membrane (ϕ_{c}) or on the tubular membrane (ϕ_{t}). The cellular density of receptors, ϕ_{c}, was quantified by relating the integrated intensity of fluorescently labeled receptors in the cell membrane to the absolute number of receptors, using a concentration calibration of free dye in solution, and subsequently dividing by the membrane area. Quantifying the density in more than 150 cells per receptor revealed that $0.001 < \phi_{\mathrm{c}} < 0.02$. This range was previously found to be within the low-density range in which the curvature-dependent sorting is not affected by the value of ϕ_{c} (refs. 27,56). We verified and tested this prediction for the Y2R (**Supplementary Fig. 2g,h**). Thus henceforth, for simplicity, we fixed $\phi_{\mathrm{c}} = 0.002$ in the model. Two approximations were taken in the above. First, in line with previous studies[57,58], we have not included a lipid area fraction factor $1 - \phi$ in the bending energy of the lipid membrane in equation (1). This is justified, as the area fraction of protein is quite small (see above), and thus the correction to the membrane bending energy is also small. In addition, this factor would not change the structure of our model (see below). It would simply redefine κ_{p} as $\kappa_{\mathrm{p}} \to \kappa_{\mathrm{p}} - \kappa$, which would have no effect on our conclusions on the effect of ligand binding on GPCR stiffness, since κ is constant.

Second, the lipid bilayer was modeled as one homogeneous elastic sheet. In reality the lipid composition is different in the two monolayers of the plasma membrane, which could affect the protein–membrane interaction across the bilayer, and thus κ_{p}. It can be shown that such a bilayer asymmetry ($\Delta\kappa_{\mathrm{p}}$) leads to an energy density term $\phi\Delta\kappa_{\mathrm{p}}e/R^3$, where e is the bilayer thickness. However, as $\Delta\kappa_{\mathrm{p}}$ is likely to be much smaller than κ_{p}, and $e << R$, the contribution from this term is assumed to be negligible compared with the other terms in equation (2), and is thus omitted for simplicity reasons.

3. Mixing energy. TMPs interact with a variety of proteins in their local environment, including other membrane proteins and cytosolic proteins. However, inhomogeneities in protein density are entropically unfavorable. To account for this mixing energy, we apply a modified Flory–Huggins model[59] that includes an entropic term and an interaction term that is assumed to be linear in ϕ (with the protein interaction coefficient α), justified by the low values of GPCR area fractions:

$$f_m(T,\phi,\alpha) = \frac{k_{\mathrm{B}}T}{a}(\phi\ln\phi + (1-\phi)\ln(1-\phi) - \alpha\phi), \tag{3}$$

where k_{B} is Boltzmann's constant, T is temperature, and a is the protein's cross-sectional area. The protein interaction term $\alpha < 0$ for repulsive interactions and $\alpha > 0$ for attractive ones. Both the cytosolic and membrane environments are expected to be different (in terms of protein and lipid content) in filopodia and cell body plasma membrane. This probably leads to a difference between protein–protein interactions in the two compartments, resulting in a different value of α on the cell body plasma membrane (α_{c}) than that on the filopodium or tether (α_{t}). The novelty in our model comes from the difference in α between cell body and filopodium: usually in solution theory[59], α is simply a constant and does not contribute to the chemical potential (see below). Combining the above energies, and neglecting plasma membrane curvature, the plasma membrane energy density is

$$f_{\mathrm{c}} = \frac{\kappa_{\mathrm{p}}}{2}\phi_{\mathrm{c}}c_{\mathrm{p}}^2 + f_{\mathrm{m}}(T,\phi_{\mathrm{c}},\alpha_{\mathrm{c}}) \tag{4}$$

Similarly, the tube energy density is

$$f_{\mathrm{t}} = \frac{\kappa}{2}\frac{1}{R^2} + \frac{\kappa_{\mathrm{p}}}{2}\phi_{\mathrm{t}}\left(\frac{1}{R} - c_{\mathrm{p}}\right)^2 + f_{\mathrm{m}}(T,\phi_{\mathrm{t}},\alpha_{\mathrm{t}}) \tag{5}$$

We assume here that the membrane is incompressible and have thus not included a membrane-stretching energy, which determines the tension σ. We note that although σ influences the tube radius, here the tube radius is measured directly, allowing us to bypass σ, in contrast with previous reports[14,56].

Protein sorting. 1. Balance of chemical potentials. The relative enrichment of TMPs on the tube at equilibrium is calculated by balancing lipid and protein chemical potentials on the plasma membrane of the cell body and on the tubular membrane protrusions. In the case of an incompressible membrane, changes in lipid and protein density are coupled and the lipid and protein chemical potentials are not mutually independent. It can, however, be shown using the approach developed previously[56] that the condition of equal chemical potentials reduces to

$$\frac{\partial f_{\mathrm{t}}}{\partial\phi_{\mathrm{t}}} = \frac{\partial f_{\mathrm{c}}}{\partial\phi_{\mathrm{c}}} \tag{6}$$

Because the plasma membrane is much larger than the tube, it can be treated as a protein reservoir and thus ϕ_{c} is constant.

2. Normalized density. With the aid of equations (3–5), the balance of chemical potentials, equation (6), leads to an implicit equation for the protein density on the tube as a function of curvature $c = 1/R$

$$\frac{1}{2}c(c - 2c_{\mathrm{p}})\frac{\kappa_{\mathrm{p}}a}{k_{\mathrm{B}}T} + \Delta\alpha - \ln\left(\frac{\phi_{\mathrm{c}}}{1-\phi_{\mathrm{c}}}\right) + \ln\left(\frac{\phi_{\mathrm{t}}}{1-\phi_{\mathrm{t}}}\right) = 0 \tag{7}$$

where $\Delta\alpha = \alpha_{\mathrm{c}} - \alpha_{\mathrm{t}}$ represents the energetic difference between protein–protein interactions taking place on the filopodia (α_{t}) and on the cell body (α_{c}) with the sign of $\Delta\alpha$ reflecting more ($\Delta\alpha > 0$) or less ($\Delta\alpha < 0$) attractive interactions in the cell body plasma membrane. Rearranging the above, the normalized density, given by $S = \phi_{\mathrm{t}}/\phi_{\mathrm{c}}$, is given by

$$S = \frac{\exp\left[-\Delta\alpha + \frac{\kappa_{\mathrm{p}}a}{k_{\mathrm{B}}T}c\left(c_{\mathrm{p}} - \frac{c}{2}\right)\right]}{1 - \phi_{\mathrm{c}} + \phi_{\mathrm{c}}\exp\left[-\Delta\alpha + \frac{\kappa_{\mathrm{p}}a}{k_{\mathrm{B}}T}c\left(c_{\mathrm{p}} - \frac{c}{2}\right)\right]} \tag{8}$$

Equation (8) is the key equation in this model and is used to fit the normalized density data as a function of c. The interaction term $\Delta\alpha$ causes non-curvature-dependent relative enrichment. We would like to emphasize that our model is phenomenological, and we do not pretend to describe the complex molecular mechanisms that are effectively contained in α.

For small curvatures, it is readily shown that S increases linearly with c, with a slope $\sim\kappa_{\mathrm{p}}c_{\mathrm{p}}$; thus the 'sorting power' is related to κ_{p} and c_{p}. Consequently, S as a function of filopodium radius can be approximated by $S = S_0 + B/R$, where S_0 is the sorting limit as the tube curvature is extrapolated to zero ($R \to \infty$) and where B is a constant. Finally, it is also apparent that S reaches a maximum at the intrinsic curvature, $c = c_{\mathrm{p}}$. **Figure 4** shows that the rate of increase of S with c decreases at larger curvatures; this is reflected in the non-monotonic behavior of $S(c)$ contained in equation (8).

We performed error-weighted numerical fits of equation (8) to the raw data sets of GPCR normalized density versus filopodia curvature. The fits were performed in Mathematica 10 version 3 (Wolfram Research, Inc.) using the NonlinearModelFit function. The error on the extracted fitting parameters represents the standard error. The error variance scale was weighted using the experimental error in the data. The raw data and the fits are plotted together in **Supplementary Figure 4**. To visualize the trend in the data we averaged the raw data into error-weighted bins ($N = 50$ to 100 points per bin). The error bars on the binned data are on the x axis the error-weighted s.d., and on the y axis the error-weighted s.e.m., quantified as an approximate ratio variance as previously described[60].

Quantification of cell membrane rigidity. To compare the extracted bending rigidity of the receptors, κ_{p}, to the bending rigidity of the cell membrane, κ, we

used a previously described method[54] to quantify κ for living cells by measuring the force necessary to extend cell membrane tethers. In brief, we pulled tethers from living HEK293 cells as described above using an optically trapped bead. As κ is purely a membrane property, we used cells treated with an actin-disrupting agent, cytochalasin, to avoid any mechanical influence of actin on the membrane. The force on the bead, F, was quantified from the displacement of the trapped bead in relation to its trap equilibrium position, and plotted for the time course of tether extraction. After an initial rise in the force when the tether is formed, the force curve reaches a plateau, in which the tether lengthens at constant pulling force, F_0. For cytochalasin-treated cells and short tethers, we can calculate κ from F_0 using the following equation[54]

$$\kappa = \frac{F_0 R}{2\pi} \qquad (9)$$

In this equation, R is the radius of the tether, which was measured for cytochalasin-treated fibroblasts as $R = 144 \pm 14$ nm.

Quantification of tether holding force. The tether force is given by $f = 2\pi\sqrt{2\kappa\sigma_t}$, and consequently a significant change in membrane rigidity (κ) or tension (σ_t) could influence the tether force. To confirm that the two ligands used in this work did not interfere with membrane physical properties we measured the tether holding force of wild-type HEK293 cells incubated with and without ligands (100 nM PYY3-36 or 100 μM ISO). Tethers of a length of 10–15 μm were pulled from the cells, and the tether force was quantified right after the tether was extracted by measuring the position of the trapped particle by using a quadrant photodiode.

Data availability. All data generated or analyzed during this study are included in this published article and its supplementary information files. Source data files for **Figures 1**–**4** are available online.

51. Pedersen, S.L. *et al.* Improving membrane binding as a design strategy for amphipathic peptide hormones: 2-helix variants of PYY3-36. *J. Pept. Sci.* **18**, 579–587 (2012).
52. Reihani, S.N.S., Mir, S.A., Richardson, A.C. & Oddershede, L.B. Significant improvement of optical traps by tuning standard water immersion objectives. *J. Opt.* **13**, 105301 (2011).
53. Richardson, A.C., Reihani, N., & Oddershede, L.B. Combining confocal microscopy with precise force-scope optical tweezers. *Proc. SPIE* **6326**, 632628 (2006).
54. Pontes, B. *et al.* Cell cytoskeleton and tether extraction. *Biophys. J.* **101**, 43–52 (2011).
55. Berk, D.A. & Hochmuth, R.M. Lateral mobility of integral proteins in red blood cell tethers. *Biophys. J.* **61**, 9–18 (1992).
56. Prévost, C. *et al.* IRSp53 senses negative membrane curvature and phase separates along membrane tubules. *Nat. Commun.* **6**, 8529 (2015).
57. Kralj-Iglic, V., Heinrich, V., Svetina, S. & Zeks, B. Free energy of closed membrane with anisotropic inclusions. *Eur. Phys. J. B* **10**, 5–8 (1999).
58. Callan-Jones, A., Durand, M. & Fournier, J.B. Hydrodynamics of bilayer membranes with diffusing transmembrane proteins. *Soft Matter* **12**, 1791–1800 (2016).
59. Dill, K.A. & Bromberg, S. *Molecular Driving Forces: Statistical Thermodynamics in Chemistry and Biology* (Garland Science, New York, 2003).
60. Gatz, D.F. & Smith, L. The standard error of a weighted mean concentration. 1. Bootstrapping vs other methods. *Atmos. Environ.* **29**, 1185–1193 (1995).